Journal of Power Sources 595 (2024) 234050

Contents lists available at ScienceDirect

Journal of Power Sources

journal homepage: www.elsevier.com/locate/jpowsour

Porosity characterisation of solid-state battery electrolyte with terahertz time-domain spectroscopy

S. Kiritharan [a], S. Lucas [b], R. Degl'Innocenti [a,1], X. Hua [c], R. Dawson [b], H. Lin [a,*]

[a] Department of Engineering, Lancaster University, Lancaster, LA1 4YW, United Kingdom
[b] LiNa Energy White Cross Industrial Estate, Unit 1 Sharpes Mill, South Road, Lancaster, LA1 4XQ, United Kingdom
[c] Department of Chemistry, Lancaster University, Lancaster, LA1 4YR, United Kingdom

HIGHLIGHTS

- Demonstrated sensitivity of terahertz radiation to NaSICON-based electrolyte.
- NaSICON densities quantified using effective medium theory.
- Estimated densities correlates to Archimedes analysis.
- Estimated densities agrees with to mercury porosimetry data.

ARTICLE INFO

Keywords:
Terahertz
THz-TDS
Porosity
NaSICON
Solid state electrolyte

ABSTRACT

With a growing interest on inorganic ceramics based solid-state electrolytes for all-solid-state batteries, there is a need to maximise their density to optimise electrochemical performance and fuel impermeability. In this paper, we demonstrate the sensitivity of terahertz time-domain spectroscopy (THz-TDS) combined with effective medium theory to quantify the porosity or density of sodium superionic conductor (NaSICON)-based solid-state electrolyte (SSEs) pellets prepared at densities in the range of 2.2–2.9 g cm^{-3}, corresponding to 50–90 % relative densities sintered at 900–1150 °C. The results of which, have been validated against complementary Archimedes analysis and mercury porosimetry highlighting the potential of THz-TDS for rapid, contactless, non-destructive electrolyte characterisation.

1. Introduction

There is a growing interest on solid-state electrolytes (SSEs) for all-solid-state batteries due to superior thermal stability, lower flammability, improved durability and potentially higher energy density [1,2]. The widely investigated SSEs generally take the form of inorganic ceramics or organic polymers where inorganic SSEs are superior in terms of ionic conductivity ($<10^{-5}$ S cm^{-1} for organic polymers compared against 10^{-3} S cm^{-1} for inorganic ceramics [3,4]). With a high stability in ambient and high temperature conditions, as well as the possibility of manufacturing at scale, inorganic solid oxides such as perovskite, sodium superionic conductor (NaSICON), lithium superionic conductor, garnet and lithium phosphorus oxynitride are considered as the closest for widespread application [5]. These solid oxide SSEs can be manufactured in a number of ways such as pressing the powder followed by thermal treatment and subsequent polishing [2] or by screen printing, atomic layer deposition and tape casting for scale-ups [6]. Common to all manufacturing strategies, there is a need to maximise the densities of solid oxide SSEs or minimise their porosities. This is important to minimise the amount of discrete grains present in the microstructure and reduce the associated grain boundaries [7] for maximising electrolytes ionic conductivity [8] and minimising fluid permeability [9–11]. In particular, grain boundaries can reduce the bulk ionic conductivity by at least an order of magnitude [12,13] and reduce fluids permeance by a factor of three [14]. The latter point is particularly important to reduce the likelihood of dendrite formation and hence the potential for cell short-circuiting and eventual device failure [15–17].

Common techniques to analyse the extent of densification of

* Corresponding author
E-mail address: h.lin2@lancaster.ac.uk (H. Lin).
[1] Present address: School of Electronic Engineering and Computer Science, Queen Mary University of London, London, E1 4NS, United Kingdom.

https://doi.org/10.1016/j.jpowsour.2024.234050
Received 6 November 2023; Received in revised form 13 December 2023; Accepted 1 January 2024
Available online 13 January 2024

inorganic ceramics SSEs include the Archimedes method, also known as hydrostatic weighing, helium pycnometry and mercury porosimetry [18,19]. Archimedes density determination is a straightforward technique that gives the sample bulk density but can be susceptible to errors such as deviating values with the presence of air bubbles at the surface, or drops of water lost upon immersing the sample [20]. Helium pycnometry flows helium through the sample to determine the skeletal volume of the solid in the sample, which is then used to calculate the bulk density of the solid, excluding the void spaces. Measurement times are typically at the minutes time scale. In contrast, mercury porosimetry applies pressurised mercury as a non-wetting liquid into the pores of a sample. As an elevated pressure is needed to force mercury into smaller pores, a pore size distribution can be produced using gradually increasing pressures, at the expense of a longer measurement time, usually in the order of hours at increased computational complexity. Owing to the use of mercury, the technique is also destructive. As both of these techniques rely on fluids entering the sample through open and connecting pores, closed pores are therefore not probed. Therefore the extracted densities tend to be an overestimate [21–23]. X-ray computed microtomography is an alternative technique that is able to measure the electron density differences of the imaged material through 3D reconstructions and can provide information on pore sizes and distributions non-invasively and non-destructively [24]. Even though this technique can provide detailed information on both closed and open pores, measurement times are typically in the order of hours, in addition to the computationally expensive image processing and tomographic reconstructions required for subsequent analysis [25]. Other techniques such as scanning electron microscopy (SEM), and X-ray diffraction (XRD) have also been used to characterise structural properties of inorganic ceramics SSEs [26–30] but the extracted information do not translate to a quantifiable measure of densification or porosity [31] thus often used to further support understanding. SEM measurements, for example allows sample morphology to be seen through cross-sectional images taken [32] while XRD is used to characterise crystallographic structures, phase purities and the level of crystallinity as a result of densification [33].

The terahertz portion of the electromagnetic spectrum is situated between 0.1 and 4 THz and can penetrate through non-metallic materials. Terahertz time-domain spectroscopy (THz-TDS) is a technique to coherently generate and detect broadband terahertz radiation. In particular, a femtosecond near-infrared pulses are focused onto a terahertz emitter, such as a semiconductor photoconductive antenna or nonlinear crystal, where each optical pulses produce sub-picosecond pulses with a frequency bandwidth from several hundred GHz to a few THz. These generated terahertz pulses in turn interact with the sample of interest where the resulting terahertz electric fields are measured by photoconduction or electro-optical detection with a coherent scheme. The key advantage of this technique is that the amplitude and phase of the terahertz pulse can both be measured for accurately extracting the sample's dielectric response in the form of complex refractive index at terahertz frequencies. This an intrinsic material property that includes refractive index and absorption coefficient. Advances in the emerging THz-TDS have opened up many exciting applications [34–38] where the link between the extracted refractive index and the porosity in organic polymer pellets have been demonstrated producing porosity data consistent with helium pycnometry [23,39]. Compared to existing techniques, THz-TDS is attractive because measurements are non-destructive, which can be taken rapidly and without physical contact. Motivated by these demonstrations, this paper explores the applicability of THz-TDS to extracting the densities of environmentally sustainable NaSICON-based SSEs.

2. Methods and materials

2.1. Pellet compaction

NaSICON powder compacts were used in this study where 500 mg of NaSICON powder was sieved through pores of 125 μm diameter and was directly compressed into flat-faced, cylindrical pellets using a manual hydraulic press (Specac, United Kingdom), using up to 0.5 tonnes of force with a minimum interval of 0.1 tonnes. The pellets had target thickness and diameter of ~2.5 mm and 12 mm, respectively. Pressed pellets were then sintered at temperatures between 900 °C to 1150 °C at 50 °C increments, omitting the temperature of 950 °C, resulting in a porosity range of 10 %–50 %. For each of the sintering temperatures investigated, there were three repeats. Prior to characterisation, these pellets were sanded down to thicknesses between 0.8 and 1.1 mm using 400 grit sandpaper, and surface polished using 1000 grit sandpaper.

2.2. Terahertz porosity analysis

THz-TDS measurements of the prepared pellets were acquired using a Tera K-15 spectrometer (Menlo Systems, Germany) in transmission (Fig. 1). Measurements were taken in ambient conditions where each waveform spanned a range of 100 ps at a time resolution of 0.033 ps. To mitigate the effect of noise and the potential for baseline drift, 500 averages were taken to represent one measurement and a free-space reference measurement was acquired immediately prior to sample measurement, respectively. Waveform recordings of the reference and sample terahertz electric field data were then fast Fourier transformed for frequency domain analysis, where the sample spectra is normalized against the reference resulting in a complex transmission function with amplitude and phase components. These are then used to extract the frequency-dependent optical constants in the form of refractive index $n(\nu)$ and absorption coefficient $a(\nu)$ using Eqs (1) and (2), respectively [40]

$$n(\nu) = 1 + \frac{c}{2\pi\nu d}\Phi(\nu) \tag{1}$$

$$a(\nu) = -\frac{2}{d}\ln\left[t(\nu)\frac{(n(\nu)+1)^2}{4n(\nu)}\right] \tag{2}$$

where ν is the corresponding frequency, c is the speed of light in vacuum (2.998×10^8 ms^{-1}), d is the thickness of the sample, $t(\nu)$ and $\Phi(\nu)$ is the amplitude ratio and phase difference between sample and reference measurements, respectively. As part of signals preprocessing, the phase needs to be unwrapped, which effectively adds or subtracts multipliers of 2π to the phase to ensure a continuous spectrum. Given that the phases are unreliable at low frequencies, extrapolations from reliable data at higher frequencies are made. For further details on processing can be found elsewhere [40]. Sample porosity can be determined from the extracted refractive index using effective medium theory provided that scattering is negligible. Examples of effective medium theory include zero porosity approximation (ZPA) or Bruggeman's Effective Medium Approximation (TB-EMA) [39] where both approaches consider two media in the sample i.e. solid electrolyte and air voids within the solid matrix. In ZPA, a linear relationship between the sample's effective refractive index to its porosity is assumed [23] and is described as the following

$$n_{eff} = n_{solid} + (1 - n_{solid})f \tag{5}$$

where n_{eff} is the effective refractive index from measurement and analysis using Eq (1), n_{solid} is the refractive index of the bulk sample with zero porosity, and f is the sample's porosity. Such a linear relationship may inaccurately estimate the porosity thus other models have also been explored [39], such as the TB-EMA model, which assumes spherical pores resulting in Eq (6) for a solid and air two-component system [39]:

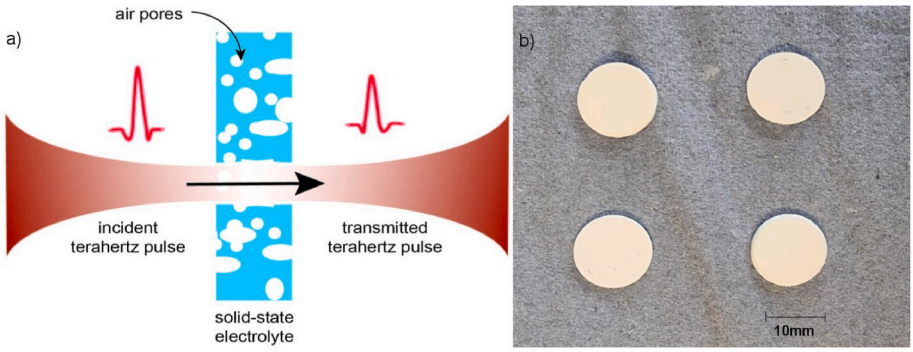

Fig. 1. (a) Schematic showing THz-TDS measurement of a SSE pellet. (b) Photo of SSE pellets.

$$\frac{n_{solid}^2 - n_{eff}^2}{n_{eff}^2 + 2\left(n_{solid}^2 - n_{eff}^2\right)}(1-f) - \frac{n_{air}^2 - n_{solid}^2}{n_{air}^2 + 2(n_{air}^2 - n_{solid}^2)}f = 0 \quad (6)$$

where n_{air} is the refractive index of air representing the inclusions within the solid. It should be noted that since there are only two components in the system, density and porosity are used interchangeably where porosity is converted to density by subtracting from 1, or 100 %. All the terahertz data analysis were processed using codes developed in Matlab (MathWorks Inc., MA, USA).

2.3. Archimedes density

An Archimedes setup is used to measure the bulk sample density and analysed using Eq 7

$$\rho_{sample} = \rho_{water}\frac{m_{air}}{m_{air} - m_{water}} \quad (7)$$

where ρ_{sample} corresponds to the density of the sample and ρ_{water} is the density of water, which takes the value of 0.998 g cm^{-3}, while m_{air} and m_{water} are mass readings of the sample when dry and suspended in water, respectively.

2.4. Electrochemical impedance spectroscopy (EIS)

A pellet sintered at each of the sintering temperatures was formed into a coin cell using layers of elemental sodium metal electrodes as the working and counter electrodes. The coin cell was pressed with a manually operated hydraulic press. To quantify the ionic conductivity of the electrolytes, EIS using SP-240 potentiostat (BioLogic, France) was performed on the coin cells at frequencies between 100 mHz and 1 MHz with an alternating current at a maximum potential difference of 10 mV for three cycles. The acquired data was fitted to a modified Randle circuit using the associated EC Lab software (BioLogic, France) to calculate the respective ionic conductivities (see SI).

2.5. X-ray diffraction (XRD)

XRD patterns were acquired on two pellets (1100 and 1150 °C) on the top surface and the middle section, made accessible after pellets were sanded down by ~13 mm, using a Rigaku Miniflex diffractometer (Rigaku Corporation, Japan) using a Cu-Kα source in the 2θ range of 12–75°. The patterns were refined using Rietveld refinement method with the Rigaku Smartlab Studio II to provide insight on the sample phase purity.

2.6. Mercury porosimetry

Measurements were acquired using PoreMaster 60 (Anton Paar GmbH, Austria) and Quantachrome PoreMaster with a pressure range of 0.904–49.895 pounds per square inch absolute (PSIA), inclusive of the atmospheric pressure. The total sample porosity is calculated by expressing the intruded volume of mercury as a proportion of the sample volume. Due to destructive nature of mercury porosimetry, only one pellet at each of the sintering temperatures with the exception of 1150 °C were analysed.

3. Results and discussion

3.1. THz-TDS

The extracted frequency-dependent effective refractive indices and absorption coefficients of the samples sintered at different temperatures are shown in Fig. 2. It should be noted that spectral oscillations observed at frequencies higher than 0.6 THz are due to noise, approaching the experimental apparatus' dynamic range. As expected, the amorphous morphology of the ceramics materials results in featureless, monotonically increasing absorption spectra, with the refractive index spectra decreasing with increasing frequency [41]. Fig. 2 further shows that the extracted optical constants generally increase with increasing sintering temperatures resulting in higher densities with the exception of the samples at 1150 °C. As refractive index is related to porosity [42], Fig. 3 shows the refractive indices at 0.4 THz as a function of sintering temperatures where a large error bar for the 1150 °C batch is observed due to thermally induced phase change at elevated temperatures (See section 3.4). The bulk solid's refractive index is estimated to be ~3.27 and is determined by extrapolating from samples' refractive indices and geometric densities for the theoretical maximum at 3.25 g cm^{-3} [43]. Fig. 3 also shows the densities of the samples analysed using both the ZPA and TB-EMA models where only a marginal difference is observed between the two models. The TB-EMA model has consistently been more accurate as the ZPA model assumes a linear relationship.

3.2. Archimedes density and mercury porosimetry

Fig. 4 compares the extracted relative densities using THz-TDS against absolute densities using Archimedes density measurements and relative densities from mercury porosimetry. It can be seen that there is a direct correlation to the absolute densities, while a close quantitative agreement with mercury porosimetry, with discrepancies possibly due to the localised nature of terahertz measurements compared to the bulk nature of these complementary measurements. As a quick check, the Archimedes density measurement value extrapolated for a 100 % dense sample is found to be ~3.10 g cm^{-3}, which is slightly lower than the prior reported theoretical maximum of 3.25 g cm^{-3} [43]. It should also be noted that comparison against Archimedes data for the outlier data points at 1150 °C is also in agreement at lower densities with similar error.

Mercury porosimetry analysis further provides insight into the relative pore size distributions, which shows that at 900 °C, the pore sizes

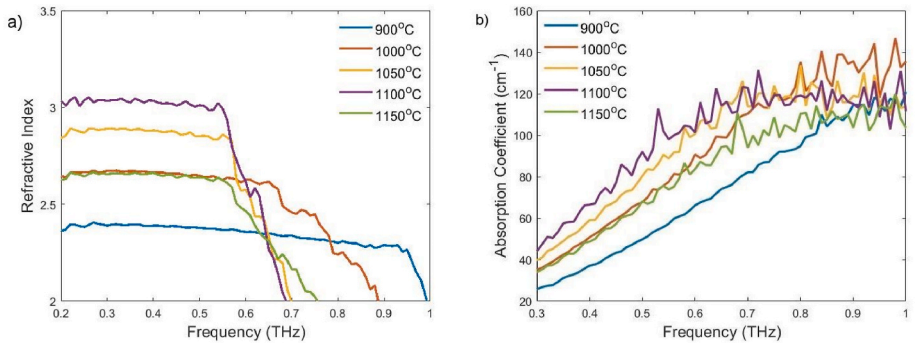

Fig. 2. (a) Effective refractive indices and (b) absorption coefficients of the sintered pellets at different temperatures.

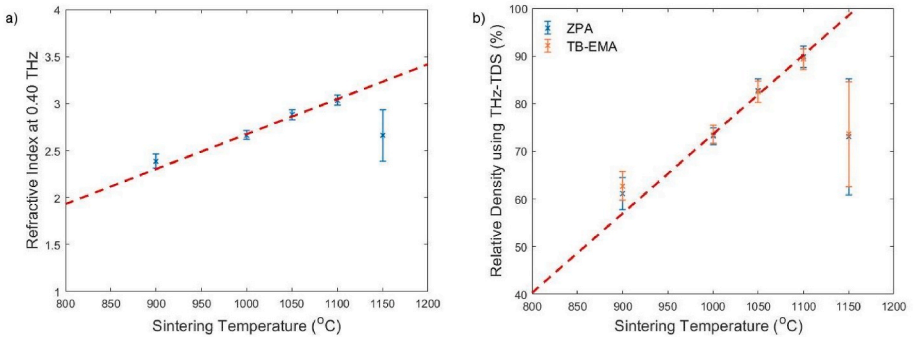

Fig. 3. (a) Effective refractive indices and (b) corresponding relative densities analysed using ZPA and TB-EMA models. Lines are plotted to guide the eye.

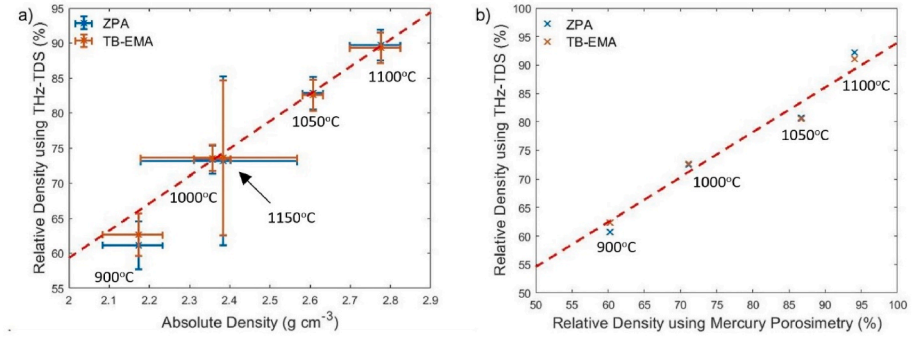

Fig. 4. Relative densities from THz-TDS against the corresponding (a) Archimedes absolute densities, and (b) relative densities using mercury porosimetry. Lines are plotted to guide the eye.

were in the range of 7 μm up to 200 μm. Upon an increasing sintering temperature, the smallest and the very largest pores were removed. As the pellets continue to densify with higher sinter temperatures, the range of pore sizes converges to 10–20 μm (see SI).

3.3. Ionic conductivity

EIS ionic conductivities are shown in Fig. 5 as a function of pellet sintering temperature, where as expected, ionic conductivities increase with increasing sintering temperatures. This increase is by more than an order of magnitude, i.e. from 1×10^{-5} S cm^{-1} at 1000 °C to 3.3×10^{-4} S cm^{-1} at 1100 °C (with the exception of 1150 °C sample, see Section 3.4). This order of magnitude of difference in conductivities is due to inclusion of grain boundaries in line with prior results [12]. The maximum measured ionic conductivity of 3.3×10^{-4} S cm^{-1} is in agreement with the previously reported value of 3.35×10^{-4} S cm^{-1} [44]. It should be noted that the 900 °C batch did not have sufficient density to withstand the pressure of coin cell preparation thus resulting in no EIS measurement.

3.4. XRD and phase change

In order to investigate the outlier data point at 1150 °C in Figs. 2–5, Fig. 6 compares the XRD patterns for the pellets sintered at 1100 °C and 1150 °C against a reference pattern of NaSICON [45] where impurities are also highlighted.

By performing a Rietveld analysis on the obtained patterns as detailed in SI, Fig. 7 compares the refined phase proportions, where apparent differences are observed. In particular, the pellet sintered at 1150 °C has a greater proportion of low density NaSICON phase 'NaSICON low' than the 1100 °C profile thus suggesting that the electrolyte has undergone phase change at this sintering temperature [46]. The phase change is also more pronounced at the middle of the pellet. The low density NaSICON phase has a calculated unit cell density of 3.09 g cm^{-3} compared to the standard phase of 3.40 g cm^{-3}, which is comparable to the theoretical maximum of 3.25 g cm^{-3} [43] but higher due

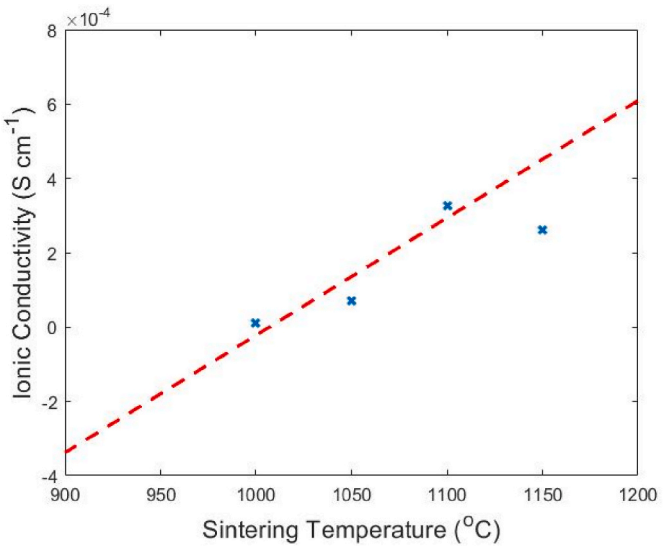

Fig. 5. EIS ionic conductivities as a function of pellet sintering temperature. Line is plotted to guide the eye.

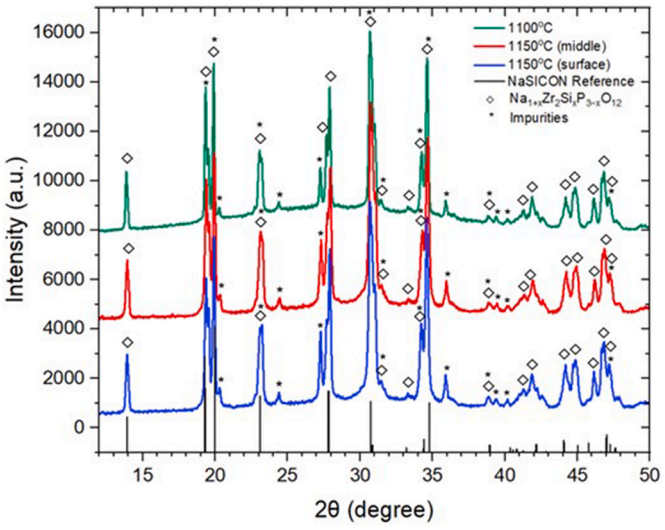

Fig. 6. XRD patterns of the pellet sintered at 1100°C and at 1150 °C at the surface and middle of the pellet. Peaks due to impurities, namely zircon ($ZrSiO_4$), silicon dioxide (SiO_2), silicon sodium and sodium oxide (Na_2O), and NaSICON ($Na_{1+x}ZrSi_xP_{3-x}O_{12}$) have been assigned. A NaSICON reference [45] is also included. (For interpretation of the references to colour in this figure legend, the reader is referred to the Web version of this article.)

to being unit cell density. The significant proportion of the lower density NaSICON phase found in the pellets sintered at 1150 °C therefore results in a lower average density as observed with Archimedes data, consistent with terahertz measurements.

3.5. Discussions

Given that there is a close agreement between the presented results against complementary Archimedes analysis and mercury porosimetry, it therefore confirms the validity of our assumption on negligible scattering at 0.4 THz or at wavelength of 750 μm. This is at least an order of magnitude greater than the 10s of μm pore sizes from mercury porosimetry (see SI). Furthermore, as TB-EMA is slightly more accurate than ZPA, our results also suggests that the pores are likely to be spherical in shape without much asymmetry. Despite the agreeable results, practitioners of the technique should generally be aware of the following: 1) THz-TDS provides only provide bulk properties but not the detailed micro-structures e.g. pore size distribution. For these information, x-ray computed microtomography and mercury porosimetry are suitable modalities though mercury porosimetry is destructive and both would require relatively long measurement and analysis times (several hours at least); 2) The sampled volume is determined by the spot size of the incident terahertz beam, which is typically at 1–2 mm but can be reduced down to sub-mm with tighter focusing [34]; 3) Determining porosity/density from extracted effective refractive indices will require effective medium theory models to be established and an estimation of bulk material refractive index, which is material dependent; 4) Owing to the strong attenuating nature of these electrolytes, sample thicknesses will be limited down to sub-mm for terahertz beam penetration thus applicable to free-standing SSEs for ex-situ characterisation. The key advantages of THz-TDS, however, are the non-destructive/non-invasive and contactless aspect the measurements, which means that different techniques can be used to study the same sample. Moreover, the rapid nature at which measurements can be acquired (10–100 ms) and analysed (several seconds) suggest that it may find use in manufacturing quality control as process in-line sensor or for inspecting spatial variations across large-area SSEs, which is becoming increasingly popular [5, 47]. At the same time, the semi-transparency of terahertz radiation to a range of materials [41], which could function as viewing windows to coin cells also highlights the potential for studying SSE's in-situ dynamics. However, such an investigation would require careful cell design, measurement and analysis, which is the subject of further study.

4. Conclusion

In this study, we have demonstrated the sensitivity of THz-TDS to resolve the porosity or density of NaSICON-based SSEs pellets prepared at densities in the range of 2.2–2.9 g cm^{-3}, corresponding to 50–90 % relative densities sintered at 900° to 1150 °C, where the results have been benchmarked against Archimedes analysis, mercury porosimetry and the consequential effect on the SSEs' ionic conductivities shown.

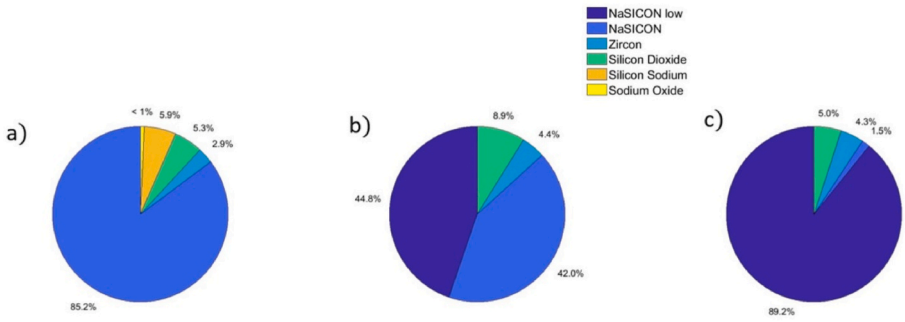

Fig. 7. Pie charts showing the phase proportion of (a) a pellet sintered at 1100 °C, the surface (b) and middle (c) of a pellet sintered at 1150 °C.

Using effective medium theory in the form of ZPA and TB-EMA, the density can be quantified at sufficient fidelity across NaSICONs. The Bruggeman model was found to be marginally closer to the true values as opposed to the ZPA approach, as a result of using an exponential relationship as opposed to ZPA's linear model. To explain the anomalous results observed at 1150 °C, XRD measurements and Rietveld analysis were used to show material phase change, which resulted in lower densities with greater variation but still observable with THz-TDS thus highlighting the robustness of the proposed approach. Without a loss of generality, the presented methodology can also be applied to other inorganic SSEs provided that they are semi-transparent to terahertz radiation. Our results show that while measurement and analysis are more complex compared to conventional techniques like Archimedes analysis and mercury porosimetry, THz-TDS is an emerging, contactless, non-destructive characterisation technique with clear potential to complement existing methods and to open up new opportunities for rapid SSE testing, enabling a greater material understanding for performance optimisation.

CRediT authorship contribution statement

S. Kiritharan: Data curation, Investigation, Resources, Software, Writing – original draft, Writing – review & editing. **S. Lucas:** Data curation, Investigation, Validation, Writing – review & editing. **R. Degl'Innocenti:** Resources, Writing – review & editing. **X. Hua:** Methodology, Supervision, Writing – review & editing. **R. Dawson:** Conceptualization, Funding acquisition, Project administration, Resources, Supervision, Writing – review & editing. **H. Lin:** Conceptualization, Funding acquisition, Methodology, Project administration, Software, Supervision, Writing – review & editing.

Declaration of competing interest

The authors declare the following financial interests/personal relationships which may be considered as potential competing interests: Hungyen Lin reports financial support was provided by Royal Academy of Engineering. Sreenivasan Kiritharan reports financial support was provided by Centre for Global Eco-Innovation. Richard Dawson reports a relationship with LiNa Energy Limited that includes: employment and equity or stocks. If there are other authors, they declare that they have no known competing financial interests or personal relationships that could have appeared to influence the work reported in this paper.

Data availability

Data will be made available on request.

Acknowledgements

SK acknowledges financial support from the Centre for Global Eco-Innovation funded by the European Regional Development Fund. HL acknowledges financial support from Royal Academy of Engineering Industrial Fellowships programme. The authors would also like to thank Dr Decio Alves de Lima for support with EIS measurements. Additional data for this manuscript is available at https://doi.org/10.17635/lancaster/researchdata/647.

Appendix A. Supplementary data

Supplementary data to this article can be found online at https://doi.org/10.1016/j.jpowsour.2024.234050.

References

[1] Q. Zhao, S. Stalin, C.-Z. Zhao, L.A. Archer, Designing solid-state electrolytes for safe, energy-dense batteries, Nat. Rev. Mater. 5 (2020) 229–252, https://doi.org/10.1038/s41578-019-0165-5.
[2] Y. Zheng, Y. Yao, J. Ou, M. Li, D. Luo, H. Dou, Z. Li, K. Amine, A. Yu, Z. Chen, A review of composite solid-state electrolytes for lithium batteries: fundamentals, key materials and advanced structures, Chem. Soc. Rev. 49 (2020) 8790–8839, https://doi.org/10.1039/D0CS00305K.
[3] T. Famprikis, P. Canepa, J.A. Dawson, M.S. Islam, C. Masquelier, Fundamentals of inorganic solid-state electrolytes for batteries, Nat. Mater. 18 (2019) 1278–1291, https://doi.org/10.1038/s41563-019-0431-3.
[4] M. Duchardt, U. Ruschewitz, S. Adams, S. Dehnen, B. Roling, Vacancy-controlled Na^{+} superion conduction in $Na_{11}Sn_2PS_{12}$, Angew. Chem. Int. Ed. 57 (2018) 1351–1355, https://doi.org/10.1002/anie.201712769.
[5] A. Chen, C. Qu, Y. Shi, F. Shi, Manufacturing strategies for solid electrolyte in batteries, Front. Energy Res. 8 (2020) 571440, https://doi.org/10.3389/fenrg.2020.571440.
[6] J.A.S. Oh, X. Xu, Z. Zeng, K. Wang, N.Y.J. Tan, E. Kok, J. Huang, L. Lu, Thin NASICON Electrolyte to Realize High Energy Density Solid-State Sodium Metal Battery, Energy & Environ Materials, 2023, https://doi.org/10.1002/eem2.12472.
[7] Y.-Y. Sun, Q. Zhang, L. Yan, T.-B. Wang, P.-Y. Hou, A review of interfaces within solid-state electrolytes: fundamentals, issues and advancements, Chem. Eng. J. 437 (2022) 135179, https://doi.org/10.1016/j.cej.2022.135179.
[8] W. Li, N. Zhao, Z. Bi, X. Guo, Insight into synergetic effect of bulk doping and boundary engineering on conductivity of NASICON electrolytes for solid-state Na batteries, Appl. Phys. Lett. 121 (2022) 033901, https://doi.org/10.1063/5.0098255.
[9] S. Lee, K. Lee, S. Kim, K. Yoon, S. Han, M.H. Lee, Y. Ko, J.H. Noh, W. Kim, K. Kang, Design of a lithiophilic and electron-blocking interlayer for dendrite-free lithium-metal solid-state batteries, Sci. Adv. 8 (2022), https://doi.org/10.1126/sciadv.abq0153 eabq0153.
[10] X. Liu, R. Garcia-Mendez, A.R. Lupini, Y. Cheng, Z.D. Hood, F. Han, A. Sharafi, J. C. Idrobo, N.J. Dudney, C. Wang, C. Ma, J. Sakamoto, M. Chi, Local electronic structure variation resulting in Li 'filament' formation within solid electrolytes, Nat. Mater. 20 (2021) 1485–1490, https://doi.org/10.1038/s41563-021-01019-x.
[11] P. Díaz-Rodríguez, M. Panizo-Laiz, C. González, R. Iglesias, I. Martín-Bragado, R. González-Arrabal, J.M. Perlado, O. Peña-Rodríguez, A. Rivera, Direct observation of hydrogen permeation through grain boundaries in tungsten, Emergent Mater 5 (2022) 1075–1087, https://doi.org/10.1007/s42247-021-00344-w.
[12] J.A. Dawson, P. Canepa, T. Famprikis, C. Masquelier, M.S. Islam, Atomic-scale influence of grain boundaries on Li-ion conduction in solid electrolytes for all-solid-state batteries, J. Am. Chem. Soc. 140 (2018) 362–368, https://doi.org/10.1021/jacs.7b10593.
[13] Y. Inaguma, C. Liquan, M. Itoh, T. Nakamura, T. Uchida, H. Ikuta, M. Wakihara, High ionic conductivity in lithium lanthanum titanate, Solid State Commun. 86 (1993) 689–693, https://doi.org/10.1016/0038-1098(93)90841-A.
[14] S. Honda, P. Jia, Y. Daiko, S. Hashimoto, B. Nait-Ali, D.S. Smith, Y. Iwamoto, Gas permeation and thermomechanical properties for macroporous alumina focused on necking size at grain boundaries, Int. J. Appl. Ceram. Technol. 19 (2022) 828–837, https://doi.org/10.1111/ijac.13860.
[15] F. Shen, M.B. Dixit, X. Xiao, K.B. Hatzell, Effect of pore connectivity on Li dendrite propagation within LLZO electrolytes observed with synchrotron X-ray tomography, ACS Energy Lett. 3 (2018) 1056–1061, https://doi.org/10.1021/acsenergylett.8b00249.
[16] Y. Uchida, G. Hasegawa, K. Shima, M. Inada, N. Enomoto, H. Akamatsu, K. Hayashi, Insights into sodium ion transfer at the Na/NASICON interface improved by uniaxial compression, ACS Appl. Energy Mater. 2 (2019) 2913–2920, https://doi.org/10.1021/acsaem.9b00250.
[17] S. Zhao, X. Zhu, W. Jiang, Z. Ji, M. Ling, L. Wang, C. Liang, Fundamental air stability in solid-state electrolytes: principles and solutions, Mater. Chem. Front. 5 (2021) 7452–7466, https://doi.org/10.1039/D1QM00951F.
[18] S. Radloff, L.S. Kremer, A. Hoffmann, M. Wohlfahrt-Mehrens, Characterization of structured ultra-thick LiNi0.6Co0.2Mn0.2O2 lithium-ion battery electrodes by mercury intrusion porosimetry, Mater. Today Commun. 28 (2021) 102549, https://doi.org/10.1016/j.mtcomm.2021.102549.
[19] T. Beuse, M. Fingerle, C. Wagner, M. Winter, M. Börner, Comprehensive insights into the porosity of lithium-ion battery electrodes: a comparative study on positive electrodes based on LiNi0.6Mn0.2Co0.2O2 (NMC622), Batteries 7 (2021) 70, https://doi.org/10.3390/batteries7040070.
[20] B. Wolf, Application of hydrostatic weighing to density determination of tiny porous samples, Rev. Sci. Instrum. 66 (1995) 2578–2581, https://doi.org/10.1063/1.1145591.
[21] M. Hasanuzzaman, A.R.M. Harunur Rashid, A.-G. Olabi, Characterization of porous glass and ceramics by mercury intrusion porosimetry, in: Reference Module in Materials Science and Materials Engineering, Elsevier, 2017 B9780128035818092663, https://doi.org/10.1016/B978-0-12-803581-8.09266-3.
[22] T.P. Santos, M. Fátima Vaz, M.L. Pinto, A.P. Carvalho, Porosity characterization of old Portuguese ceramic tiles, Construct. Build. Mater. 28 (2012) 104–110, https://doi.org/10.1016/j.conbuildmat.2011.08.004.
[23] D. Markl, P. Wang, C. Ridgway, A.-P. Karttunen, M. Chakraborty, P. Bawuah, P. Pääkkönen, P. Gane, J. Ketolainen, K.-E. Peiponen, J.A. Zeitler, Characterization of the pore structure of functionalized calcium carbonate tablets by terahertz time-

domain spectroscopy and X-ray computed microtomography, J. Pharmaceut. Sci. 106 (2017) 1586–1595, https://doi.org/10.1016/j.xphs.2017.02.028.
[24] L. Farber, G. Tardos, J.N. Michaels, Use of X-ray tomography to study the porosity and morphology of granules, Powder Technol. 132 (2003) 57–63, https://doi.org/10.1016/S0032-5910(03)00043-3.
[25] S. Schlüter, A. Sheppard, K. Brown, D. Wildenschild, Image processing of multiphase images obtained via X-ray microtomography: a review, Water Resour. Res. 50 (2014) 3615–3639, https://doi.org/10.1002/2014WR015256.
[26] J.A.S. Oh, L. He, A. Plewa, M. Morita, Y. Zhao, T. Sakamoto, X. Song, W. Zhai, K. Zeng, L. Lu, Composite NASICON ($Na_3Zr_2Si_2PO_{12}$) solid-state electrolyte with enhanced Na^+ ionic conductivity: effect of liquid phase sintering, ACS Appl. Mater. Interfaces 11 (2019) 40125–40133, https://doi.org/10.1021/acsami.9b14986.
[27] M. Abdulai, K.B. Dermenci, S. Turan, SPS sintering and characterization of Li7La3Zr2O12 solid electrolytes, MRS Energy & Sustainability (2022), https://doi.org/10.1557/s43581-022-00055-7.
[28] E. Hayakawa, H. Nakamura, S. Ohsaki, S. Watano, Characterization of solid-electrolyte/active-material composite particles with different surface morphologies for all-solid-state batteries, Adv. Powder Technol. 33 (2022) 103470, https://doi.org/10.1016/j.apt.2022.103470.
[29] Y. Subramanian, R. Rajagopal, K.-S. Ryu, Synthesis, air stability and electrochemical investigation of lithium superionic bromine substituted argyrodite (Li6-xPS5-xCl1.0Brx) for all-solid-state lithium batteries, J. Power Sources 520 (2022) 230849, https://doi.org/10.1016/j.jpowsour.2021.230849.
[30] D. Wagner, J. Schilm, C.W. Lee, M. Kusnezoff, Impact of precrystallized $NaYSi_4O_{12}$ powders in the synthesis of sodium conducting solid electrolytes, Energy Technol. 8 (2020) 2000559, https://doi.org/10.1002/ente.202000559.
[31] M. Soweizy, M. Zahedifar, M. Karimi, Fabrication and characterization of Ag-doped Li1.3Al0.3Ti1.7(PO4)3 solid electrolyte with high ionic conductivity, J. Mater. Sci. Mater. Electron. 31 (2020) 9614–9621, https://doi.org/10.1007/s10854-020-03504-6.
[32] F. Zhu, H. Bao, X. Wu, Y. Tao, C. Qin, Z. Su, Z. Kang, High-performance metal–organic framework-based single ion conducting solid-state electrolytes for low-temperature lithium metal batteries, ACS Appl. Mater. Interfaces 11 (2019) 43206–43213, https://doi.org/10.1021/acsami.9b15374.
[33] P. Yadav, M.C. Bhatnagar, Structural studies of NASICON material of different compositions by sol–gel method, Ceram. Int. 38 (2012) 1731–1735, https://doi.org/10.1016/j.ceramint.2011.09.022.
[34] H. Lin, B.M. Fischer, S.P. Mickan, D. Abbott, in: S.F. Al-Sarawi (Ed.), Review of THz Near-Field Methods, 2006, p. 64140L, https://doi.org/10.1117/12.695309. Adelaide, Australia.
[35] H. Lin, B.P. Russell, P. Bawuah, J.A. Zeitler, Sensing water absorption in hygrothermally aged epoxies with terahertz time-domain spectroscopy, Anal. Chem. 93 (2021) 2449–2455, https://doi.org/10.1021/acs.analchem.0c04453.
[36] H. Lin, O.J. Burton, S. Engelbrecht, K.-H. Tybussek, B.M. Fischer, S. Hofmann, Through-substrate terahertz time-domain reflection spectroscopy for environmental graphene conductivity mapping, Appl. Phys. Lett. 116 (2020) 021105, https://doi.org/10.1063/1.5135644.
[37] D.F. Alves-Lima, X. Li, B. Coulson, E. Nesling, G.A.H. Ludlam, R. Degl'Innocenti, R. Dawson, M. Peruffo, H. Lin, Evaluation of water states in thin proton exchange membrane manufacturing using terahertz time-domain spectroscopy, J. Membr. Sci. 647 (2022) 120329, https://doi.org/10.1016/j.memsci.2022.120329.
[38] D.Y.S. Chau, A. R Dennis, H. Lin, J. Axel Zeitler, A. Tunnacliffe, Determination of water content in dehydrated mammalian cells using terahertz pulsed imaging: a feasibility study, Chem. Pharm. Bull. 17 (2015) 200–207, https://doi.org/10.2174/1389201017666151029105941.
[39] P. Bawuah, D. Markl, D. Farrell, M. Evans, A. Portieri, A. Anderson, D. Goodwin, R. Lucas, J.A. Zeitler, Terahertz-based porosity measurement of pharmaceutical tablets: a tutorial, J. Infrared, Millim. Terahertz Waves 41 (2020) 450–469, https://doi.org/10.1007/s10762-019-00659-0.
[40] M. Naftaly, Terahertz Metrology, Artech House, Norwood, Massachusetts, 2014.
[41] M. Naftaly, R.E. Miles, Terahertz time-domain spectroscopy for material characterization, Proc. IEEE 95 (2007) 1658–1665, https://doi.org/10.1109/JPROC.2007.898835.
[42] P. Bawuah, K.-E. Peiponen, A terahertz time-domain study on the estimation of opto-mechanical properties of pharmaceutical tablets using the Hashin–Shtrikman bounds for refractive index: a case study of microcrystalline cellulose and starch acetate compacts, Opt. Rev. 23 (2016) 502–509, https://doi.org/10.1007/s10043-016-0198-6.
[43] L. Shen, J. Yang, G. Liu, M. Avdeev, X. Yao, High ionic conductivity and dendrite-resistant NASICON solid electrolyte for all-solid-state sodium batteries, Mater. Today Energy 20 (2021) 100691, https://doi.org/10.1016/j.mtener.2021.100691.
[44] A.G. Jolley, G. Cohn, G.T. Hitz, E.D. Wachsman, Improving the ionic conductivity of NASICON through aliovalent cation substitution of Na3Zr2Si2PO12, Ionics 21 (2015) 3031–3038, https://doi.org/10.1007/s11581-015-1498-8.
[45] H. Y-P, L. Laboratory, Crystal Structures and Crystal Chemistry in the System Nal+xZr2SixP3_xO12, (n.d.).
[46] C. Wen, Z. Luo, H. Liang, X. Liu, W. Lei, A. Lu, Effect of sintering temperature and holding time on the crystal phase, microstructure, and ionic conductivity of NASICON-type 33Na2O-40ZrO2-40SiO2-10P2O5 solid electrolytes, Appl. Phys. A 128 (2022) 71, https://doi.org/10.1007/s00339-021-05219-9.
[47] K.B. Hatzell, Y. Zheng, Prospects on large-scale manufacturing of solid state batteries, MRS Energy & Sustainability 8 (2021) 33–39, https://doi.org/10.1557/s43581-021-00004-w.